Numerical study of melting of a phase change material (PCM) enhanced by deformation of a liquid-gas interface

Yangkyun Kim, Akter Hossain, Yuji Nakamura

Division of Mechanical and Space Engineering. Hokkaido University. N 13, W 8, Kita-Ku. 060-8628. Sapporo. Japan.

ABSTRACT

Numerical simulations are performed in order to examine the time-dependent melting, and heavily deforming processes of phase change material (PCM) subjected to local heating. By comparing cases with and without deformation, the impact of the inclusion of a deformation model is firstly addressed to understand what influences the precise melting behavior. Mass, momentum and energy conservation equations are solved in a 2-D system based on a fixed grid by means of a finite volume method. The Volume of Fluid (VOF) method and the Enthalpy-Porosity method are applied to model the deformable liquid-gas interface and the melting processes, respectively. Results successfully show the melting, subsequent deformation and dropping-off behavior of the molten PCM. It is found that the inclusion of the deformation model enhances the melting owing to the increase of the total received heat; namely, widening of the contact area at the melting front and induced flow motion inside molten PCM improve the heat transfer toward the melting front. Parametric studies by varying the applied Stefan number so as to change the surface tension are also made to ensure the above-mentioned enhancement mechanism is universally applicable.

Keywords:

Free surface moving
Enthalpy-Porosity method
Melting
Numerical modeling
Volume of fluid (VOF)

NOMENCLATURE

A_{mush}	morphology constant, kg/(m^3 s)
c_p	specific heat at constant pressure, J/(kg K)
$\mathbf{F}_{ST}$	surface force (*per unit volume*), N/m^3
$\mathbf{g}$	gravity acceleration, m/s^2
ΔH	latent heat, J/kg
h	enthalpy, J/kg
h_{ref}	reference enthalpy, J/kg
k	thermal conductivity, W/(m K)
L	latent heat of fusion, J/kg
$\mathbf{n}_s$	interface normal
P	pressure, Pa
Ste	Stefan number (c_p ($T_E - T_{liquidus}$) / L)
S_H	volumetric source for latent heat, W/m^3
$\mathbf{S}_M$	sink term (*per unit volume*), N/m^3
T	temperature, K
T_E	temperature of external thermal input, K
$T_{liquidus}$	liquidus temperature, K
$T_{solidus}$	solidus temperature, K
T_{ref}	reference temperature, K
t	time, s
$\mathbf{v}$	velocity, m/s

V_A	initial volume of air, m^3
V_{PA}	pendant and detached liquid volume in initial volume of air, m^3
V_{SP}	volume of solid state PCM, m^3
V_{TP}	total volume of PCM, m^3

Greek symbols

α	volume fraction
α_P	averaged pendant volume fraction
β	liquid fraction
β_L	averaged liquid volume fraction
$\Delta\beta_L$	deviation of the averaged liquid volume fraction between the cases of deformable and non-deformable PCM-air interface
δ_s	Dirac function
ε	computational constant (0.001)
κ_c	curvature of free surface, 1/m
μ	viscosity, kg/(m s)
ρ	density, kg/m^3
σ	surface tension coefficient, N/m

Subscript

A	air
g	gas
L-PCM	liquid state PCM
l	liquid
m	melting
mush	mushy zone
PA	pendant and detached molten PCM
ref	reference
S-PCM	solid state PCM
SP	solid state PCM
TP	total PCM

1. Introduction

Combustion over insulated electric wire has been investigated as an important fire safety issue in connection with a variety of aspects of building fires. According to reported statistics, fires involving electrical wiring account for 13,000 fires and $ 0.5 billion in property loss during a year in USA [1] and account for 3 % (971 cases) of all fires in Japan [2]. Thus it is desirable to prevent fires through an accurate understanding of their causes. Over the past few decades, a series of experimental studies on burning behavior of electric wire has been conducted, providing a rich experimental database [3-6]. In particular, Nakamura et al. studied flame spread over electric wires insulated by polyethylene (PE) under sub-atmospheric pressure in normal gravity [7-9], and reported that molten PE significantly deformed and eventually dropped from the bulk of the insulation during the spreading event (see Fig. 3 in [8]). The timing of the dropping off of PE was not random, but rather was periodic, and the frequency depended on the applied environmental conditions such as the type of burning materials. Importantly, this observation of significant PE-deformation concerns two major problems involved in predicting the associated fire hazard. One is the non-steadiness of the spreading rate owing to the continuous change of the size of the molten PE caused by frequent accumulation and dropping off [9]. This is important in fire science because a steady fire spread rate can be treated as the system eigenvalue, simplifying the determination of analytical or numerical solutions. The second is the enlargement of fire damage, not limited to the region around the cable but also extending to the space underneath owing to the dropping of the PE. In particular, the temperature of the PE must be higher than its gasification temperature at 622 K in the absence of surrounding flames, and could be up to 800 K in their presence. Understanding the enlargement of fire damage in three dimensions is an important issue for establishing better safety strategies to prevent the growth of fire. Hence the precise prediction of dropping timing is crucial; this can be done by evaluating the heat transfer during the processes of melting and dropping off.

Numerical observation is advantageous since it is hard to track the complete history of melting in experiment. However, only a few numerical attempts have been made on this subject because of the complexity of the numerical modeling representing the melting and dynamic behavior simultaneously. Zheng et al. [10-12], numerically investigated diffusion flame over a solid surface and the associated melting effect, showing that an increase of Stefan number increases the flame spread rate and the size of the flame. However, their focus was limited to the energy change caused by melting under a flat surface with constant density, and no consideration of fluid motion was made, either inside or on the molten surface. Schiller et al. [13] and Di Blasi [14-15] simulated flame spread over liquid fuel with the inclusion of surface tension effects, and revealed that considerable motion near the gasifying surface ahead of flame is initiated by thermo-capillary flow. Obviously this study of liquid combustion did not involve melting. More recently, Butler et al. [16] and Oñate et al. [17] successfully simulated the time-dependent behavior of melt flow and gasification of polymeric materials exposed to radiant heating using the Particle Finite Element Method (PFEM). Their numerical results revealed that PFEM can calculate both melting and dynamic motion of polymers. However, their simulation did not include a precise analysis of heat transfer associated with melting. At present, therefore, the impact of the inclusion of deformation in the melting and dropping processes is not fully understood, especially with regards to the effect of abrupt dynamic motion on melting. It is therefore strongly desirable to compare two generic cases for modeling, i.e. with and without (dynamic) deformation, in order to examine whether enhanced heat transfer occurs and whether it significantly modifies the melting process or not.

In this work, we consider the most fundamental case, namely, no species transport and chemical reaction are taken into account and only heat and mass transfers play a major role in dynamic motion effect on melting. The problem then becomes a phenomenon of pure melting and dynamic motion without flaming. In this regard, the governing equations can only consist of the fundamental conservation equations (for mass, momentum and energy) under a multi-phase framework. We use the Enthalpy-Porosity [18-19] and Volume of Fluid methods (VOF) [20] in order to model the melting and dynamic motion of molten matter suspended from a metal plate. This simplified geometry provides a physically similar analogy of the wire combustion case (see, e.g., [7-9]). We also investigate the role of abrupt dynamic motion on melting through the time-dependent total heat flux on the melting front, and thereby gauge whether the inclusion of deformation enhances the melting or not. The variation of the averaged liquid volume fraction in time is also examined by adopting different Stefan numbers and surface

tension forces in order to verify the generality of above-mentioned feature. This study is done with commercial software (FLUENT 12.0) based on the finite volume method [21].

2. Mathematical and numerical model

Our numerical model calculates the time-dependent melting, deforming and dropping processes to enable the investigation of the effect of abrupt deformation of phase change material (PCM) attached beneath a solid metal plate during melting. The target phenomenon in this study involves two moving interfaces: the melting front mainly driven by energy absorption and the liquid-gas interface driven by momentum balance. In order to calculate the melting front involving solid-liquid and liquid-gas interface, Enthalpy-Porosity method (for details, see [18-19]) and Volume of Fluid (VOF) method (for details, see [20]) were employed, respectively. By exploiting a combination of these methods, melting combined with a three-phase problem was properly considered. In order to reduce the numerical difficulty in calculating the transport properties, a piecewise polynomial approximation was applied that takes into account jumps of material properties between solid-liquid phases. Note that PCM represents the universal expression of any meltable material including general polymers, and the transient range between solid and liquid has the same physical meaning as the mushy zone in metallic alloy.

2.1. Governing equations

We use continuum mechanics to model the melting, deforming and dropping PCM induced by localized thermal input. The process is governed by a set of balance equations involving the one-field assumption inside the PCM and air with an appropriate jump condition by implementing volume-averaging principle with phase indicator function. We restrict our treatment to constant material properties in each phase, assuming Newtonian fluid behavior, and neglecting the effect of compressibility, viscous dissipation and temperature effect in the bulk phases. The interfaces between gas and other materials are assumed to be sharp enough to take account of the singular characteristics of the problem [22], under the assumption that the representative volume element is small enough to resolve the interface topology. However, due to the characteristics of the mushy region between the solid and liquid, this region is modeled by assuming a thick interface [18]. This is illustrated for the case of the spatial density distribution near the interface in the schematic of Fig. 1.

Under these conditions, the governing equations for mass, momentum and energy are

$$\nabla \cdot (\mathbf{v}) = 0, \tag{1}$$

$$\frac{\partial(\rho \mathbf{v})}{\partial t} + \nabla \cdot (\rho \mathbf{v} \otimes \mathbf{v}) = -\nabla p + \nabla \cdot [\mu(\nabla \mathbf{v} + \nabla \mathbf{v}^T)] + \mathbf{F}_{ST} + \rho \mathbf{g} + \mathbf{S}_M, \tag{2}$$

$$\frac{\partial(\rho h)}{\partial t} + \nabla \cdot (\rho \mathbf{v} h) = \nabla \cdot (k \nabla T) - S_H. \tag{3}$$

Here, ρ, $\mathbf{v}$, p, h, T and α are, respectively, density, velocity, pressure, sensible enthalpy, temperature and volume fraction. μ, $\mathbf{g}$ and k are viscosity, acceleration of gravity and conductivity, respectively. The RHS of the momentum equation (Eq. (2)) consists of a surface force, $\boldsymbol{F}_{\mathrm{ST}}$, and sink term, $\boldsymbol{S}_{\mathrm{M}}$, as well as pressure gradient, viscosity and gravitational force. Since phase change is not considered at the interface between the gas and the solid or liquid, we assume that there is no flow across the interface. According to the interfacial momentum balance, momentum flux, which is introduced from the bulk phases during volume averaging, balances with the surface force, $\boldsymbol{F}_{\mathrm{ST}}$ (third term of RHS in Eq. (2)). This force is modeled as a continuum surface force (CSF), as proposed by Brackbill et al. [23], and this force is specified as a volumetric source term in the momentum equation:

$$\mathbf{F}_{ST} = \frac{\rho}{0.5(\rho_g + \rho_l)} (\sigma \kappa_c \mathbf{n}_s) \delta_s \quad \text{with} \quad \mathbf{n}_s = \frac{\nabla \tilde{\alpha}}{|\nabla \tilde{\alpha}|}. \tag{4}$$

Here, σ and δ_s are the surface tension coefficient and Dirac's delta function at the interface, and the subscripts g and l denote the gas and liquid phases, respectively. $\mathbf{n}_s$ is the interfacial unit normal, which determines the orientation of the curve within the cell that contains the interface. For better accuracy and robustness in the calculation, smoothed (filtered) volume fraction $\tilde{\alpha}$ is used in the definition of the unit normal. Smoothed volume fraction is calculated as follows: first the volume fraction at the cell corners is reconstituted by using the value stored at the cell center. Then, taking the average reconstituted volume fraction at the cell corners, the smoothed volume fraction at the cell center is obtained again. κ_c is the curvature of the free surface, and is defined in terms of the divergence of the interfacial unit normal, $\mathbf{n}_s$:

$$\kappa_c = \nabla \cdot \mathbf{n}_s. \tag{5}$$

The position of the free surface between the gas and the adjacent material is implicitly calculated by the VOF method through the phase indicator function in addition to the momentum equation. The phase indicator function, α, takes the value 0 for the gas and 1 for other phases. From mass balance in the absence of generation and consumption, this scalar quantity α should satisfy the following transport equation:

$$\frac{D\alpha}{Dt} = \frac{\partial(\alpha)}{\partial t} + \nabla \cdot (\mathbf{v}\alpha) = 0. \tag{6}$$

Here zero on the RHS stands for no gasification. The indicator function in each computational cell corresponds to the phase volume fraction which is either purely representative of the phase or of the interface depending upon the volume fraction value:

$$\alpha = \begin{cases} 1 = \textit{liquid or solid}, \\ 0 < \alpha < 1 = \textit{the cell contains the interface}, \\ 0 = \textit{gas}. \end{cases} \tag{7}$$

The momentum equation, Eq. (2), is solved for the gas, liquid and mushy regions according to the one-field assumption under the volume averaging framework [24-25]. To do so, we assume that the velocity and mixture pressure is shared in each phase. In particular, we assume that the spatial distribution of solid and liquid in the mushy region are homogeneously distributed and that solid fragments in the mushy region are shrunk or dissipated from the macroscopic points of view. Given these restrictions, the microscopic momentum equation becomes a macroscopic equation with an additional sink term, $\boldsymbol{S}_\mathrm{M}$ as last term in Eq. (2), where

$$\mathbf{S}_M = -A_{mush} \frac{(1-\beta)^2}{(\beta^3 + \varepsilon)} \mathbf{v}. \tag{8}$$

Here, A_{mush} is a constant (1.0×10^6 (kg/(m^3 s)) accounting for the mushy region morphology. Since there is no universal value for A_{mush} in modelling by Enthalpy-Porosity method, different values have been used in different systems [19, 26]. As clearly shown in [27], melt fraction and solid shape evolution are highly dependent on A_{mush}, and there exists an optimum value of A_{mush} for each system. Thus, careful determination of correct A_{mush} for our system is necessary. In this study, we choose 1.0×10^6 (kg/(m^3 s) as A_{mush} because melting behaviour is reasonably realized for our system. ε is a representive small value (0.001) introduced to prevent the numerical singularity at $\beta = 0$. β is the fraction of liquid in the cell, which behaves effectively as a porous media [18]. Mathematically, this $\boldsymbol{S}_\mathrm{M}$ term arises from the dissipative interfacial stress during the volume averaging process [28], and is modelled as a momentum sink term using a knowledge of the permeability of the porous medium [29]. Diverse modelling approaches to deal with such a permeability tensor have been studied in research on porous media [30-32]. In this study we represent it as a type of Carman-Kozeny permeability tensor [33]. As described in Ref. [19], the basic principle underlying the force $\mathbf{S}_\mathrm{M}$ relates to a gradual increase in velocity from zero in the solid to a finite value in the liquid over the cells that are undergoing a phase change. Thus when $\beta = 1$ the sink term becomes zero, and the general momentum equation is solved for the liquid, but when $\beta \neq 1$ the permeability

tensor dominates over the transient, convective and diffusive term, and the momentum equation becomes identical to the so-called Carman-Kozeny equation.

In the energy equation, h is the sensible enthalpy, given by

$$h = h_{ref} + \int_{T_{ref}}^{T} c_p dT, \tag{9}$$

where, h_{ref} is the reference enthalpy, T_{ref} is the reference temperature and c_p is the specific heat (at constant pressure). S_H is a volumetric source that takes into account the latent heat defined as

$$S_H = \frac{\partial(\rho \Delta H)}{\partial t} + \nabla \cdot (\rho \mathbf{v} \Delta H). \tag{10}$$

ΔH is defined as $\Delta H = \beta L$, where L is latent heat of melting and β is the liquid fraction that determines whether a computational cell is solid or not. β is a function of temperature, and can be described as

$$\beta = \begin{cases} 0 \ if \ T < T_{solidus}, \\ 1 \ if \ T > T_{liquidus}, \\ (T - T_{solidus}) / (T_{liquidus} - T_{solidus}) \ if \ T_{solidus} < T < T_{liquidus}, \end{cases} \tag{11}$$

where $T_{solidus}$, solidus temperature, is defoned as temperature at which melting of PCM begins. $T_{liquidus}$, liquidus temperature, is the temperature at which PCM is completely melted.

In addition to the interfacial volumetric source term as a jump condition, several additional conditions at the interfaces are necessary to achieve a mathematical solution. Concerning the flow condition, we first assume that there is no flow in the solid phase as well as in the vicinity of the solid surface, so that there is no flow jump across the solid-liquid interface. Since no phase change occurs at the gas-liquid and gas-solid interfaces, no flow exists across these interfaces. Thus the interfacial normal velocity of the fluids is equal to the normal velocity of the bulk phases at the gas-liquid and gas-solid interfaces. For point where a molten PCM/air interface meets a copper surface, we assume that the contact angle is 90 degrees, which could exclude any adhesion effect (i.e., the interface is normal to the adjacent copper surface). As the thermal boundary condition, two-side heat balance (the so-called conjugated heat transfer condition) is considered at the solid-liquid interface:

$$k_{copper} \frac{\partial T}{\partial y} = k_{PCM} \frac{\partial T}{\partial y}. \tag{12}$$

Material properties are phase-dependent values, determined by phase indicator function, α, and temperature dependent liquid fraction, β, as

$$\begin{aligned} &\rho = \alpha_{PCM} \rho_{PCM} + \alpha_g \rho_g, \ \mu = \alpha_{PCM} \mu_{PCM} + \alpha_g \mu_g, \\ &k = \alpha_{PCM} k_{PCM} + \alpha_g \kappa_g, c_p = \alpha_{PCM} c_{p,PCM} + \alpha_g c_{p,g}. \end{aligned} \tag{13}$$

Where,

$$\begin{aligned} &\rho_{PCM} = \rho_{S-PCM} + \beta(\rho_{S-PCM} - \rho_{L-PCM}), \ \mu_{PCM} = \mu_{L-PCM}, \\ &k_{PCM} = k_{S-PCM} + \beta(k_{S-PCM} - k_{L-PCM}), \ c_p = c_{p,\,S-PCM} + \beta(c_{p,\,S-PCM} - c_{p,\,L-PCM}). \end{aligned} \tag{14}$$

Thus, one can be simplify as

$$
\begin{aligned}
\rho &= \alpha_{PCM}\left(\rho_{S-PCM} + \beta(\rho_{S-PCM} - \rho_{L-PCM})\right) + \alpha_g \rho_g, \\
\mu &= \alpha_{PCM}\mu_{PCM} + \alpha_g \mu_g, \\
k &= \alpha_{PCM}\left(k_{S-PCM} + \beta(k_{S-PCM} - k_{L-PCM})\right) + \alpha_g \kappa_g, \\
c_p &= \alpha_{PCM}\left(c_{p,\,S-PCM} + \beta(c_{p,\,S-PCM} - c_{p,\,L-PCM})\right) + \alpha_g c_{p,g}.
\end{aligned}
\tag{15}
$$

All properties used in the present study are summarized in Table 1.

2.2. Computational details

The physical configuration is schematically illustrated in Fig. 2. The 2-D computational domain consists of copper, PCM and air. The total horizontal and vertical lengths are 8.0 and 7.0 cm respectively, and the thickness of the PCM is 0.5 cm. A normal downwardly-directed gravity field is considered (with corresponding gravitational acceleration 9.81 m/s^2). A localized external thermal input at temperature 500 K is placed on the top surface of the copper to initiate melting of the PCM, and the temperature 300 K is used over the whole domain as the initial thermal condition. The melting process evolves with an increase of the local temperature in the PCM. As the volume of molten PCM increases, the liquid-gas interface starts to severely deform, and PCM is eventually detached from the main part of the molten PCM owing to gravity. We assumed that the solid is homogeneously distributed in the mushy region.

Time integration is performed by a first-order explicit Euler method incorporating a variable time stepping method dependent on the local CFL condition [21]. The discretization of the convective term was done using a second-order scheme, and the diffusive term in the equations was evaluated using a central-differencing scheme. The SIMPLE scheme was used for pressure-velocity coupling. PRESTO (the Pressure Staggering Option) was used to interpolate the pressure at the face from the cell-center values [34]. For the transport of the volume fraction α, the flux was calculated in a geometrical way by the use of a PLIC (a Piecewise Linear Interpolation Calculation) to avoid numerical diffusion [35].

3. Results and discussion

In this paper, we limit the discussion to the effect of the abrupt deformation of the molten PCM up to first falling, since quite complicated phenomena (i.e., re-solidification, tiny second dropping of molten PCM, and breaking molten PCM film on the copper surface etc.) appear after that.

In our previous study [36], 2-D calculation results for convection-diffusion melting in a gallium cavity was performed with the identical modeling method and compared with the experimental result of Gau and Viskanta [37]. Good agreement of these numerical simulations with experiment were obtained (see [36]), validating the numerical model applied in the present work.

3.1 General observation on the time dependent melting and dropping

Fig. 3 shows a scalar distribution, $(\alpha + \beta)/2$, with and without consideration of deformable PCM-air interface to visualize the overall process of the melting and dropping. The white, red, green and blue colors correspond to computational cells filled with copper, air, molten PCM and solid PCM, respectively. Fig. 3a clearly shows how the PCM is melting and growing. The PCM starts to melt with the appearance of a mushy region on the upper-right side, and melting proceeds after that. At around 2.8 s, the interface between the molten PCM and the air tends to deform with increase of volume of the molten region, and because of this deformation the volume of molten PCM on the right is forced to move left. At the same time, molten PCM starts to grow in size, resulting in a pinching of the fluid neck between the main and suspended PCM. Eventually, generated molten PCM is detached from the main part, and soon disappears from computational domain. At 3.75 s, a liquid spot between the detached and cone-shaped molten PCM is maintained along the un-melted (solid) part. According to Fig. 3, it is hard to distinguish whether the spot is a satellite droplet [38] or a thin line representing a point of singularity in the diameter [39-41], because typically a satellite droplet is very small (e.g., possessing a

volume less than 1% of that of the detached molten matter [42]) and also a point of singularity (e.g., a micro-thread) that approaches its limiting size of the order of 1 μm [43]. To simulate such satellite droplets or points of singularity satisfactorily, the fixed grid resolution should be fine enough. Because our interest here is limited to the pre-dropping process, the details of the tiny secondary droplet and the point of singularity are out of the scope of this paper.

Fig. 4 shows the temperature distribution at the same times shown in Fig. 3a. The position of the melting front and the liquid-gas interface are approximated by β = 0.5 and α = 0.5, respectively. Heat generated from the external thermal input diffuses by conduction first through the copper and is absorbed in the PCM to initiate the melting, and is then released to the ambient air. Following the deformation of the free surface triggered by a volume increase of the molten area, the temperature profile also becomes distorted. In particular, the temperature profile tends to spread out as molten PCM drops off.

The volume increase of the molten and suspended, molten PCM are illustrated in Fig. 5. This figure depicts the time-dependent variation of the averaged pendant volume fraction and the averaged liquid volume fraction, defined as follows:

$$\text{Averaged pendant volume fraction}: \alpha_P = V_{\mathrm{PA}} / V_A, \tag{16}$$

$$\text{Averaged liquid volume fraction}: \beta_L = 1 - V_{SP} / V_{TP}. \tag{17}$$

Here, V_{PA} is the volume of pendant and detached molten PCM in the initial volume of air, V_{A} is the initial volume of air, V_{SP} is the volume of the solid-state PCM, and V_{TP} is the total volume of PCM. The averaged pendant volume fraction (α_P) represents the volume of pendant or detached molten PCM within the computational space, and is calculated by counting how much liquid volume is projected toward the air domain. More precisely, we calculate the volume of cells filled with liquid PCM inside the initially given total number of cells filled with gas, and then this quantity is divided by the initial volume of gas. The averaged liquid volume fraction, β_L, represents how much PCM is melted in total volume of PCM, including the mushy region as part of the molten PCM.

The averaged pendant volume fraction (α_P) keeps zero till 2.8 s, then the associated acceleration area is suddenly increased owing to a loss of equilibrium of the forces at the PCM-air interface. Eventually it suddenly decreases from its maximum value at around 3.75 s (as shown) while the suspended molten PCM is dropping. The sudden decrease in the averaged pendant volume fraction (α_P) does not count the volume of detached PCM. As can be seen from the distribution of the averaged liquid volume fraction (β_L), melting initiates at around 0.3 s, and then continuously increases although the increment gradually becomes gentle. This “bending” feature arises from (1) the position of heat source being fixed at right upper side, and (2) the heat transferred from external thermal input not only being used to enhance the melting, but also being released into the air. Immediately before dropping of molten PCM at around 3.75 s, β_L locally increases, but after dropping-off it momentarily plateaus. This increase and momentarily plateau of β_L offers the key to an understanding of the role of the dynamic motion effect on melting. In section 3.2 we will discuss this process in more detail.

3.2. Effect of abrupt dynamic motion on melting fraction

3.2.1. Heat transfer in case with and without deformable PCM-air interface during dynamic motion

In order to get insight into effect of the abrupt dynamic motion on melting, we performed the simulation *without* deformation of molten matter: namely, the melting is assumed to occur without any local volume change of the molten PCM. In Fig. 6, the dashed line stands for the time-dependent variation of the liquid volume fraction for a fixed position of the PCM-air interface, and the solid line represents the case of a deformable interface. After a time of 2.8 s, coincident with the acceleration region shown with the averaged pendant volume fraction in Fig. 5, the deviation of the averaged liquid volume fraction (β_L) is initiated with and without consideration of deformable PCM-air interface. Fig. 6 shows the maximum deviation, at a time when the molten PCM starts to drop off. This means that the abrupt dynamic motion of the molten PCM locally enhances the melting. After the detachment of molten PCM, the deviation of β_L from the cases with and without deformable PCM-air interfaces decreases owing to the loss of molten PCM in which heat has accumulated.

The local enhancement of melting by dynamic motion can be explained through the heat balance at the melting front and at the copper-PCM interface. In order to investigate this heat balance, the time-dependent total heat flux distributions at a specified line on the copper-PCM interface and at the melting front are shown in Fig. 7. The specified line is defined by a liquid fraction ranging from $\beta = 0.0$ to $\beta = 0.5$. The red and blue colors stand for the heat flux at the copper-PCM interface and at the melting front, respectively. The solid and dashed lines correspond to cases with and without a deformable PCM-air interface, respectively. As can be seen in this figure, the total heat flux at different locations has the same order of magnitude, revealing that the total heat flux at both the specified line on the copper-PCM and the melting front have a significant effect on the melting rate. Keeping these facts in mind, when we look at the case of a non-deformable PCM-air interface (dashed lines) after 0.9 s, the total heat flux at the specified line on the copper-PCM interface is always higher than that at the melting front. In other words, the heat transfer from the copper is relatively stronger than that from the melted PCM during the melting process after 0.9 s. In contrast, the case of a deformable PCM-air interface represented by solid lines in Fig. 7 shows that total heat flux at the melting front becomes higher than at the specified line after 3.2 s. This indicates that the heat transfer from liquid PCM to the melting front is stronger than that from the copper during the deforming and dropping process. According to the time-dependent total heat flux distribution, the liquid fraction of deformable PCM-air interface becomes higher than that of the non-deformable interface during deformation. The range of the liquid fraction ($0.0 < \beta < 0.5$) is intentionally selected in order to investigate heat transfer process in molten PCM so that heat flux could be changed with change of the range of the liquid fraction. However, qualitative arguments are invariant.

3.2.2. Heat transfer through the copper-PCM interface

One can see from Fig. 7 that the total heat flux of the deformable PCM-air interface at the specified line on the copper-PCM interface (see the red solid line) decreases with time after 2.8 s as compared to that of the non-deformable case. This is caused by the heat transfer through the copper-PCM interface. Fig. 8 depicts the velocity vectors in the vicinity of the deformed PCM at 3.3 s, where the color represents the magnitude of the velocity. Although the maximum velocity appears along the PCM-air interface while the molten PCM is moving, we can clearly see that the amount of fluid motion inside the molten PCM is toward to melting front. Such fluid motion conveys heat and potentially enhances the melting. Fig. 9 shows the surface heat flux along the copper-PCM interface in cases (a) without and (b) with the deformable PCM-air interface. The surface heat flux directed from the copper to PCM is defined as positive. Due to the fixed position of the thermal input, the surface heat flux tends to decrease in time both with and without a deformable PCM-air interface. However, as seen at 3.5 and 3.7 s in Fig. 9b, a negative heat flux, i.e. directed from PCM to the copper, is only found at the surface adjacent to the molten PCM. Such negative heat transfer is more clearly seen in Fig. 10, which shows the temperature distribution without and with the deformable PCM-air interface along the surface. The solid and dashed lines, respectively, represent a position corresponding to a vertical 1-mm distance from the copper-PCM interface to the copper and to the PCM at a time of 3.5 s. In the case without the deformable PCM-air interface, the conductive heat is always transferred from the copper to PCM, since the heat conduction from a localized thermal input through the copper is higher than that of the PCM. In contrast, the case with the deformable PCM-air interface shows a negative heat flux (see the range between 5.8 and 6.5 cm). Since these cases differ in whether the motion of PCM-air interface is considered, this proves that the negative heat flux is driven by the convection induced by the fluid motion of the molten PCM. In particular, the negative heat flux nearly disappears below 400 K, which corresponds to the melting temperature in this calculation. Even though flow could appear in the mushy region, its effect is not strong compared with the effect of the conduction from the copper to PCM. Thus the convective heat transfer, which can change the direction of heat transfer to work against conduction from the copper to PCM, only occurs in completely molten PCM. Consequently, Figs. 8-10 reveal that the convective heat transfer in PCM induced by collapse of the PCM-air interface initiates the negative heat flux in the molten PCM, resulting in heat loss to the copper. This is directly reflected by the differences in heat flux on the specified line of the copper-PCM interface between these two cases, as shown in Fig. 7.

3.2.3 Heat transfer through melting front

In Fig. 7, the total heat flux of the deformable PCM-air interface at the melting front increases form 2.8 s to 3.8 s compared to that of the non-deformable case. Such a sudden increase of heat flux might be caused by the following two effects. The first is the effect of the internal liquid convection inside the molten PCM initiated by the deforming and dropping process. As mentioned in 3.2.1, since the temperature of the bulk molten PCM is higher than that in the vicinity of the melting front, the fluid motion in the molten PCM can deliver the heat to sustain the high temperature gradient in the vicinity of the melting front while the molten PCM is moving and dropping. The second is the effect of length increase of melting front. Fig. 11 shows the time-dependent length distribution of the melting front for the cases with (solid line) and without (dashed line) a deformable PCM-air interface. As shown in the inset in Fig. 11, the melting front first propagates left and downward. However, once the melting front reaches the PCM-gas interface, the melting front mainly propagates to the left while losing heat toward the air. Thus the length of the melting front increases sharply up to 1.1 s, and then decreases until the time of deformation, 2.8 s. After this time, the length of the melting front increases until the dropping of molten PCM, because the suspended molten PCM, which has a relatively high temperature compared to the solidus temperature (350 K), increases the contact area between solid and liquid PCM. Therefore, an increase of the length of the melting front gives a better chance of transferring heat from the suspended molten PCM to the melting front.

3.3 Behavior of time-dependent liquid fraction for the various Stefan numbers and surface tension coefficients

Calculations were performed both in the cases with and without a deformable PCM-air interface for various Stefan numbers and surface tension coefficients. The Stefan number is defined as $Ste = c_p(T_E - T_{Liquidus})/L$, where, T_E is the temperature of the external thermal input. Figs. 12 and 13 show the time-dependent distributions of the averaged liquid volume fraction (β_L) for various Stefan numbers and surface tension coefficients, respectively. The solid and dashed lines, respectively, stand for the cases with and without a deformable PCM-air interface. Since melting could occur very quickly under the combustion condition as compare with general slow melting process (e.g. ice melting, melting in thermal storage system), high Stefan number is considered in Fig. 12. As expected, it is shown that β_L increases with increasing Stefan number in Fig. 12. This trend is consistent with the results of Hirata [42] and Assis [43], showing that the larger the ratio of sensible heat to the latent heat of fusion of the material, the higher the melting rate. Hence, the volume of accumulated molten PCM should grow more quickly with increase of the Stefan number. Consequently, dropping is quickly experienced at high Stefan number.

Fig. 13 clearly shows that a change in the averaged liquid volume fraction (β_L) for the various surface tension coefficients only occurs when dynamic motion exists; since a higher surface tension creates a higher internal pressure, molten PCM can be suspended along the copper surface longer and more easily. A high surface tension coefficient evidently delays the dropping time, as can be seen in Fig. 14. It is found in particular that β_L in case of a deformable PCM-air interface is always higher than that of non-deformable PCM-air interface over the chosen range of Stefan numbers and surface tension coefficients. Although after the molten PCM drops off several complicated physical processes simultaneously appear (as mentioned at beginning of Section 3) and the heat balance at all interfaces is sharply changed, one can conclude from this study that abrupt dynamic motion always enhances the melting rate compared with the case of a non-deformable PCM-air interface. In general, we can conclude that a consideration of the dynamic motion effect associated with melting is highly desirable for better predictions of heat transfer at melting surfaces in order to understand the dropping timing.

3.4 Effect of abrupt dynamic motion on melting rate for different Stefan number and surface tension

Results concerning the effect of abrupt dynamic motion on melting, in particular the difference of the averaged liquid volume fraction $\Delta\beta_L$ between the cases of deformable and non-deformable PCM-air interface at the time of dropping of molten PCM, are shown in Fig. 15 over a range of Stefan numbers and surface tension coefficients. We expect $\Delta\beta_L$ to arise purely from the effect of deforming and dropping of molten PCM. In Fig. 15, $\Delta\beta_L$ is seen to become larger when the applied Stefan number is either small (< 2) or large (> 5). Large Stefan number results in an increase in the temperature gradient in molten PCM, an effect which contributes the further melting. This is consistent with the previous works [46-48]. In case of small Stefan number, the length of the melting

front increases, as shown in Fig. 16. Even if conduction is not prominent, the increase of $\Delta\beta_L$ results in an enhancement in the melting rate. Fig. 15 also clearly shows that an increase in surface tension results in an increase in $\Delta\beta_L$, this is because, as explained in Section 4.3, a large surface tension results in a longer suspension time for the molten PCM. The length of the melting front therefore becomes larger, as can be seen in Fig. 16.

4. Conclusions

The time-dependent melting and dropping processes involving three phases was numerically investigated by a set of balance equations derived from local instantaneous bulk conservation equations with appropriate jump conditions using the VOF coupled with the Enthalpy-Porosity methods under a volume-averaging framework. The effect of the deformation of the liquid-gas interface on melting was precisely investigated. The following conclusions can be drawn.

1. The deformable PCM-air interface enhances the melting from the time of deformation to that of dropping as compared with the case that of a non-deformable PCM-air interface.
2. The enhancement of the melting rate associated with a deformable PCM-air interface is mainly caused by considerable internal liquid motion in the PCM triggered by surface fluid motion and an increase of surface area of the melting front during the deforming and dropping processes.
3. Noticeable heat loss from the PCM to the copper is present while the deformed molten PCM undergoes dropping. This reduced the melting rate, but this as was relatively small effect compared to the enhanced melting rate owing to convection and the increase of surface area.
4. For varying surface tension coefficients and Stefan numbers, the melting rate in the case of a deformable PCM-air interface is always higher than that of a non-deformable PCM-air interface, suggesting that the inclusion of the deformation model is essential for a proper understanding and prediction of melting.
5. The pure effect of deformation, described as $\Delta\beta_L$, in this study, increased with increase in surface tension owing to the increase of length of the melting front, with Stefan number lager than 5 owing to an increase of the convection effect, and with Stefan number smaller than 2 due to an increase in length of the melting front.

We can conclude through this study that the VOF method coupled with the Enthalpy-Porosity method can deal with the dynamic behavior of multiphase flow involving phase transitions. Current numerical models thus have the potential to model combustion in multiphase conditions. In future, the dynamic contact angle, which is not considered in this study, could be included in the modeling because it is expected to play a role in wire combustion.

ACKNOWLEDGMENTS

This work has been supported by JSPS (Grants-in-aid for Young Scientists: #21681022; PI: YN) & Japan Nuclear Energy Safety Organization (JNES) monitored by Dr. Susumu Tsuchino. We would like to express our sincere appreciation to Prof. Sungcho Kim (Sunchon National University, Korea) for his kind assistance on providing us an enrich computational environment, and to the Ministry of Education, Culture, Sports, Science and Technology, Japan for offering to YK the Monbu-kagaku-sho (MEXT) Scholarship for conducting this research. Prof. Oliver B Wright from Hokkaido University gave us valuable professional advices and kindly polished our manuscript.

REFERENCES

[1] Electrical Fire safety, 2011. <http://www.usfa.fema.gov/citizens/home_fire_prev/elecrical.shtm>.
[2] Fire and Disaster Management Agency, 2010. <http://www.fdma.go.jp/>.
[3] M. Kikuchi, O. Fujita, K. Ito, A. Sato, T. Sakuraya, Experimental study on flame spread over wire insulation in microgravity, Proc. Combust. Int. 27 (2) (1998) 2507-2514.
[4] O. Fujita, K. Nishizawa, K. Ito, Effect of low external flow on flame spread over polyethylene-insulated wire

in microgravity, Proc. Combust. Int. 29 (2) (2002) 2545-2552.
[5] O. Fujita, T. Kyono, Y. Kido, H. Ito, Y. Nakamura, Ignition of electrical wire insulation with short-term excess electric current in microgravity, Proc. Combust. Int. 33 (2) (2011) 2617-2623.
[6] M. K. Kim, S. H. Chung, O. Fujita, Effect of AC electric fields on flam spread over electrical wire, Proc. Combust. Int. 33 (1) (2011) 1145-1151.
[7] Y. Nakamura, N. Yoshimura, T. Matsumura, H. Ito, O. Fujita, Opposed-wind effect on flame spread of electric wire in sub-atmospheric pressure, J. Thermal. Sci. Tech. 3 (3) (2008) 430-441.
[8] Y. Nakamura, N. Yoshimura, H. Ito, K. Azumaya, O. Fujita, Flame spread over electric wire in sub atmospheric pressure, Proc. Combust. Int. 32 (2) (2008) 2559-2562.
[9] Y. Nakamura, K. Azumaya, H. Ito, O. Fujita, Time-dependent flame spread behavior of electric wire in sub-atmospheric pressure, 9th ASPAC. Taipei, Taiwan, 2009, 101-104.
[10] G. Zheng, I. S. Wichman, A. Benard, Opposed flow flame spread over polymeric materials, Combust. Flame 124 (2001) 387-408.
[11] G. Zheng, I. S. Wichman, A. Benard, Opposed flow ignition and flame spread over melting polymers with Navier Stokes gas flow, Combust. Theory Model. 6 (2002) 317-337.
[12] G. Zheng, I. S. Wichman, A. Benard, Energy balance analysis of ignition over a melting polymer subjected to a high radiation heat flux in a channel cross flow, Fire Safety J. 38 (2003) 229-256.
[13] D. N. Schiller, H. D. Ross, W. A. Sirignano, Computational analysis of flame spread across alcohol pools, Combust. Sci. Technol. 118 (4-6) (1996) 203-255.
[14] C. Di Blasi, S. Crescitelli, G. Russo, Model of oscillatory phenomena of flame spread along the surface of liquid fuels, Comp. Meth. App. Mech. Eng. 90 (1991) 643-657.
[15] C. Di Blasi, On the role of surface-tension-driven flow in the uniform, near-flash flame spread over liquids, Combust. Sci. and Tech. 110-111 (1995) 555-561.
[16] KM. Butler, E. Õnate, SR. Idelsohn, R. Rossi, Modeling polymer melt flow using the particle finite element method, Eleventh International Interflam Conference, London, England, 2007, 929-940.
[17] E. Õnate, R. Rossi, S. R. Idelsohn, K. M. Butler, Melting and spread of polymers in fire with the particle finite element method, Int. J. Numer. Metho. Engng. 81 (2010) 1046-1072.
[18] V. R. Voller, A fixed grid numerical modeling methodology for convection-diffusion mushy region phase-change problems, Int. J. Heat Mass Transfer 30 (1987) 1709-1719.
[19] A. D. Brent, V. R. Voller, K. J. Reid, The enthalpy-porosity technique for modeling convection-diffusion phase change: Application to the melting of a pure metal. Num. Heat Transf. 13 (1988) 297-318.
[20] C. W. Hirt, B. D. Nichols, Volume of Fluid (VOF) method for the dynamics of free boundaries, J. Comp. Phys. 39 (1981) 201-225.
[21] Fluent 12. 0 User's Guide, Available from http://www.ansys.com.
[22] M. Ishii, Thermo-fluid dynamic theory of two-phase flow, Eyrolles, Paris, 1975.
[23] J. U. Brackbill, D. B. Kothe, C. Zemach, Continuum method for modeling surface tension, J. Comp. Phys. 100 (1992) 335-354.
[24] D. A. Drew, Mathematical modeling of two-phase flow, Ann Rev Fluid Mech. 15 (1983) 261-291.
[25] C. Beckermann, R. Viskanta, Mathematical modeling of transport phenomena during alloy solidification, Appl. Mech. Rev. 46 (1993) 1-27.
[26] E. Assis, L. Katsman, G. Ziskind, R. Letan, Numerical and experimental study of melting in a spherical shell, Int. J. Heat Mass Transfer 50 (2007) 1790-1804.
[27] H. Shmueli, G. Ziskind, R. Letan, Melting in a vertical cylindrical tube: numerical investigation an coparison with experiments, Int. J. Heat Mass Transfer 53 (2010) 4082-4091.
[28] J. Ni, C. Beckermann, A volume-averaged two-phase model for solidification transport phenomena, Metall. Trans. B. 22B (1991) 349-361.
[29] S. Whitaker, Flow in porous media I: A theoretical derivation of Darcy's law, Transp. Porous Media. 1 (1986) 3-25.
[30] D. R. Poirier, S. Ganesan, Permeabilities for flow of interdendritic liquid in equaxial structures, Mater. Sci. Eng. A. 157 (1992) 113-123.

[31] C. Y. Wang, S. Ahuja, C. Beckermann, H. C. de Groh. Multiparticle interfacial drag in equiaxed solidification, Metall. Mater. Trans B. 26 (1995) 111-119.
[32] B. Goyeau, D. Benihaddadene, D. Gobin, M. Quintard. Numerical calculation of the permeability in a dendritic mushy zone, Metall. Mater. Trans B. 30 (1999) 613-622.
[33] F. J. Valdes-Parada, J. A. Ochoa-Tapia, J. Alverez-Ramirez. Validity of the permeability Carman-Kozeny equation: A volume averaging approach, Physica A. 388 (2009) 789-798.
[34] S. V. Patankar. Numerical heat transfer and fluid flow, Hemisphere. (1980) New York.
[35] D. L. Youngs. Time dependent multimaterial flow with large fluid distortion, Numer. Methods for Fluids Dynamics, edited by K.W.Morton and M.J.Baines. (1982) 273-285.
[36] Y. K. Kim, A. Hossain, S. Kim, Y, Nakamura. A numerical study on time-dependent melting and deformation processes of Phase Change Material (PCM) induced by localized thermal input, Two phase flow, Phase Change and Numerical Modeling, Intech Open Access Publisher. 23, 2011, pp. 523-540.
[37] C. Gau, R. Viskanta. Melting and solidification of a pure metal on a vertical wall, J. Heat Transfer. 108 (1986) 174-181.
[38] D. B. Bogy. Drop formation in a circular liquid jet, A. Rev. Fluid Mech. 11 (1979) 207-228.
[39] X. D. Shi, M. P. Brenner, S. R. Nagel. A cascade of structure in a drop falling from a faucet, Science. 265 (1994) 219-222.
[40] J. Egger, T. F. Dupont. Drop formation in a one-dimensional approximation of the Navier-Stokes equation, J. Fluid Mech. 262 (1994) 205-221.
[41] J. Egger, E. Villermaux. Physics of liquid jets, Rep. Prog. Phys. 71 (2008) 107-122.
[42] X. Zhang. Dynamics of growth and breakup of viscous pendant drops into air, J. Colloid Interface Sci. 212 (1999) 107-122.
[43] T. A. Kowalewski. On the separation of droplets from a liquid jet, Fluid Dyn. Res. 17 (1996) 121-145.
[44] T. Hirata, Y. Makino, Y. Kaneko. Analysis of natural convection melting inside isothermally heated horizontal rectangular capsule, Wärme- und Stoffübertrag. 28 (1993) 1-9.
[45] E. Assis, G. Ziskind, R. Letan. Numerical and experimental study of solidification in a spherical shell, ASME J. Heat Transf. 131 (2009) 309-315.
[46] J.M. Khodadadi, Y. Zhang, Effect of buoyancy-driven convection on melting within spherical containers, Int. J. Heat Mass Transfer 44 (2001) 1605-1618.
[47] T.J. Scanlon, M.T. Stickland, A numerical analysis of buoyancy-driven melting and freezing, Int. J. Heat Mass Transf. 47 (2004) 429-436.
[48] J. Virag, M. Živić, A, Galović, Influence of natural convection on the melting of ice block surrounded by water on all sides, Int. J. Heat Mass Transfer 49 (2006) 4106-4115.

List of Figure captions

Fig. 1 Concept of a thick interface at the melting front (left) and a thin interface at the free surface (right)

Fig. 2 Schematic illustration of the computational domain

Fig. 3 Distribution of $(\alpha + \beta)/2$ in case with/without deformable PCM-air interface with respect to time

Fig. 4 Time-dependent temperature distributions

Fig. 5 Time-dependent averaged liquid volume fraction of PCM and averaged pendant volume fraction of PCM

Fig. 6 Time-dependent averaged liquid volume fraction distribution with and without deformable PCM-air interface

Fig. 7 Time-dependent heat flux at copper-PCM interface (black) and melting front (blue) with and without deformable PCM-air interface (For interpretation of the references to color in this figure legend, the reader is referred to the web version of this article)

Fig. 8 Velocity distribution inside molten PCM at 3.3 s

Fig. 9 Surface heat flux distribution along copper-PCM interface for cases (a) without and (b) with considering deformable PCM-air interface over time

Fig. 10 Temperature at a point which is 1 mm away from copper-PCM interface toward copper side (solid line) and PCM side (dashed line) at 3.5 s

Fig. 11 Time-dependent distribution of the length of the melting front with and without a deformable PCM-air interface

Fig. 12 Time-dependent liquid fraction distribution for various Stefan numbers at surface tension coefficient = 0.25

Fig. 13 Time-dependent liquid fraction distribution for various surface tension coefficient at *Ste* = 0.68

Fig. 14 Time-for deformation and dropping according to surface tension coefficient at *Ste* = 0.68

Fig. 15 Difference of averaged liquid volume fraction between cases of deformable and non-deformable PCM-air interface for various Stefan numbers and surface tension coefficients at the time of dropping

Fig. 16 Length of melting front according to surface tension coefficient and Stefan number at the time of dropping

Table caption

Table 1 Physical properties used in the present calculation

Figures

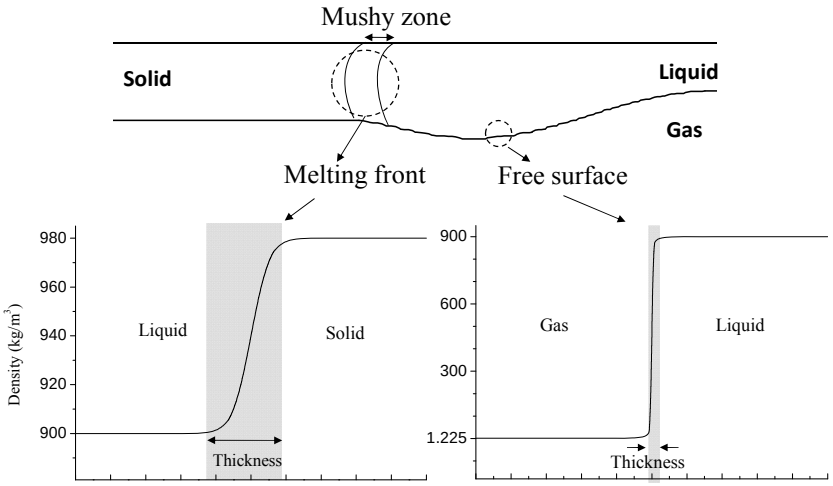

Fig. 1 Concept of a thick interface at the melting front (left) and a thin interface at the free surface (right)

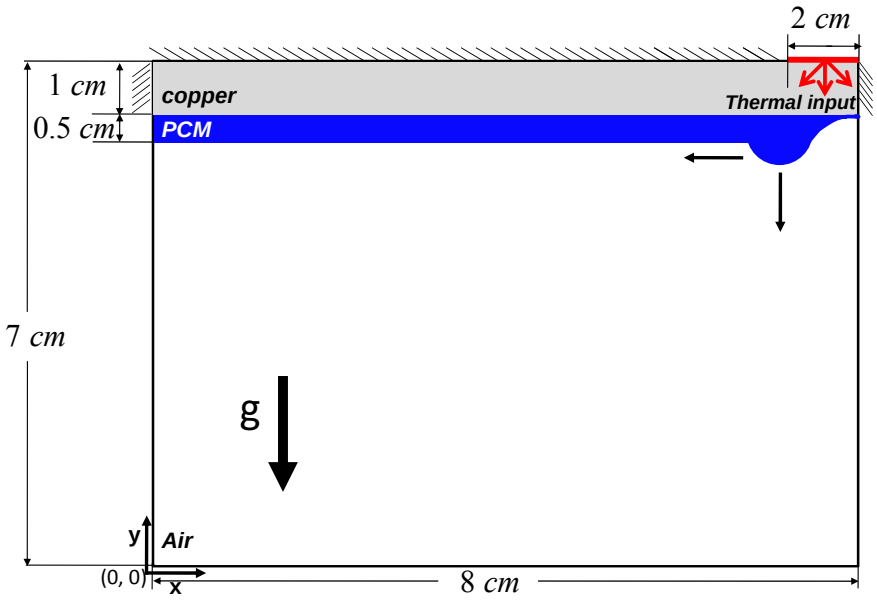

Fig. 2 Schematic illustration of the computational domain

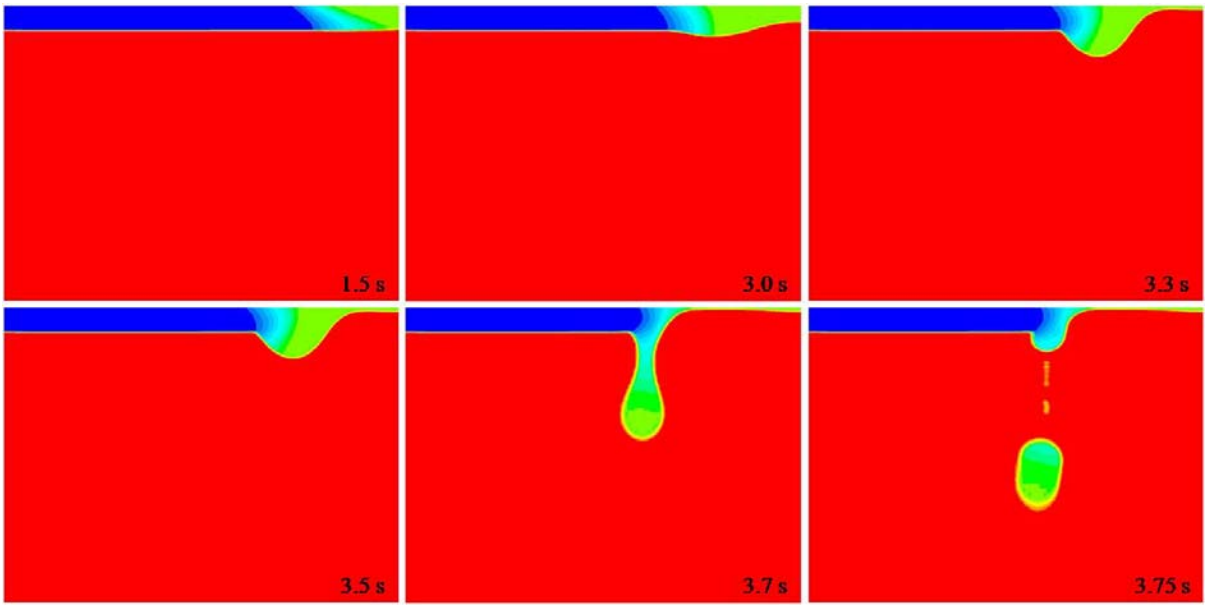

(a) Case with deformable PCM-air interface

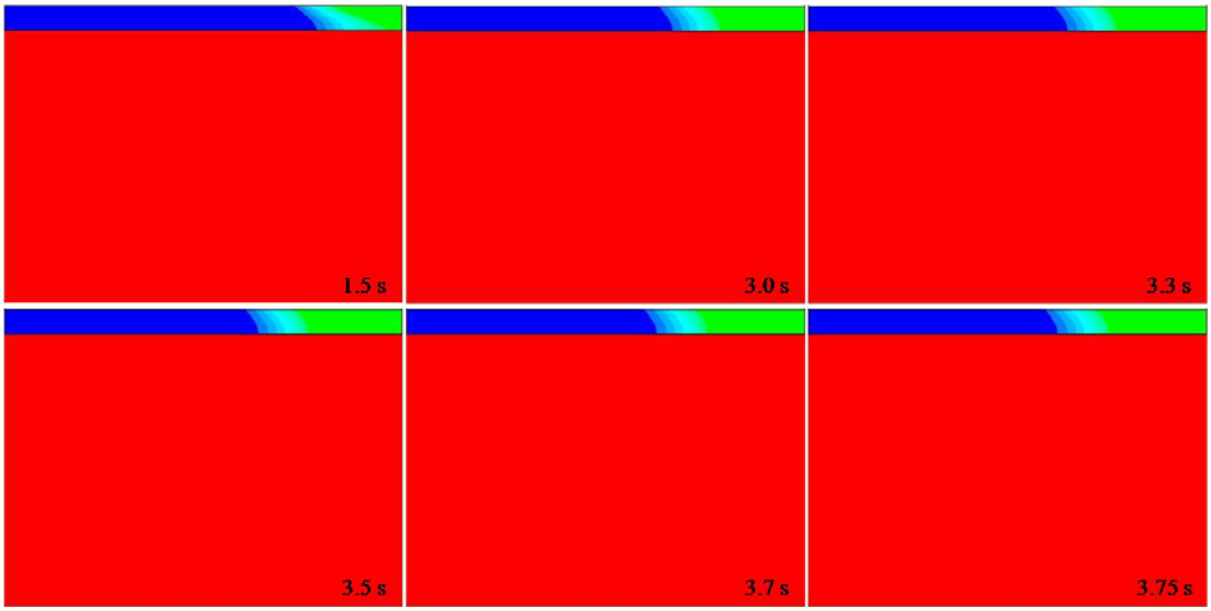

(b) Case without deformable PCM-air interface

Fig. 3 Distribution of $(\alpha + \beta)/2$ in case with/without deformable PCM-air interface with respect to time

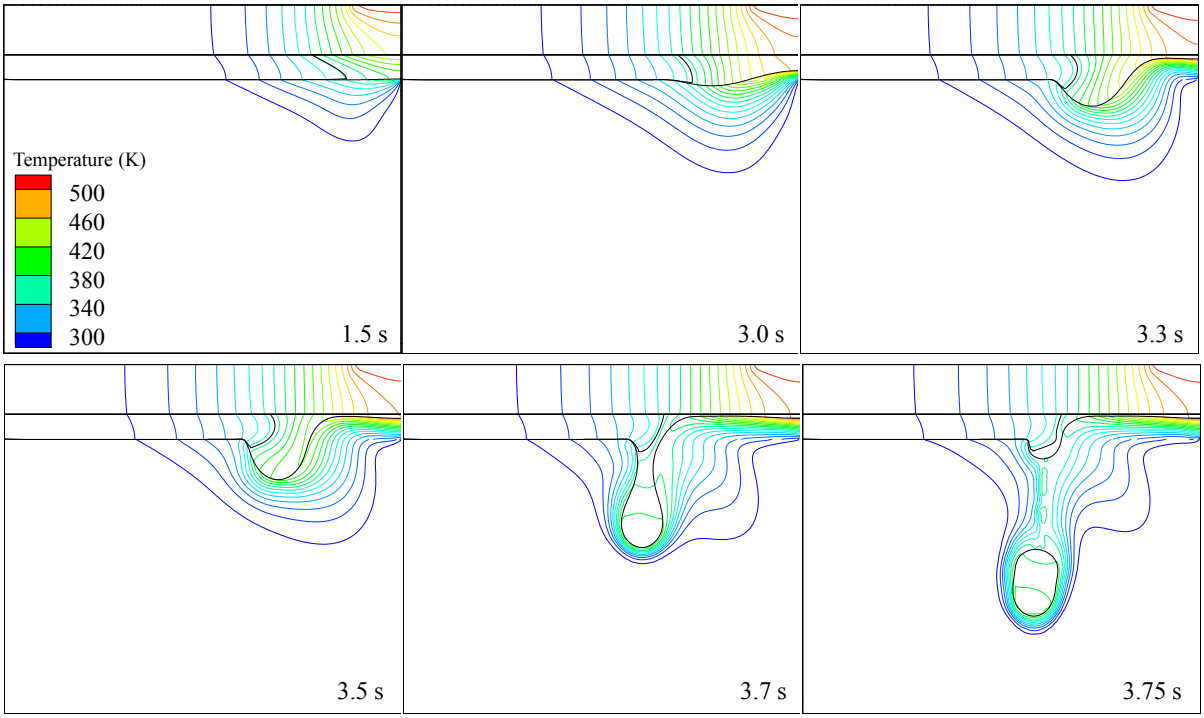

Fig. 4 Time-dependent temperature distributions

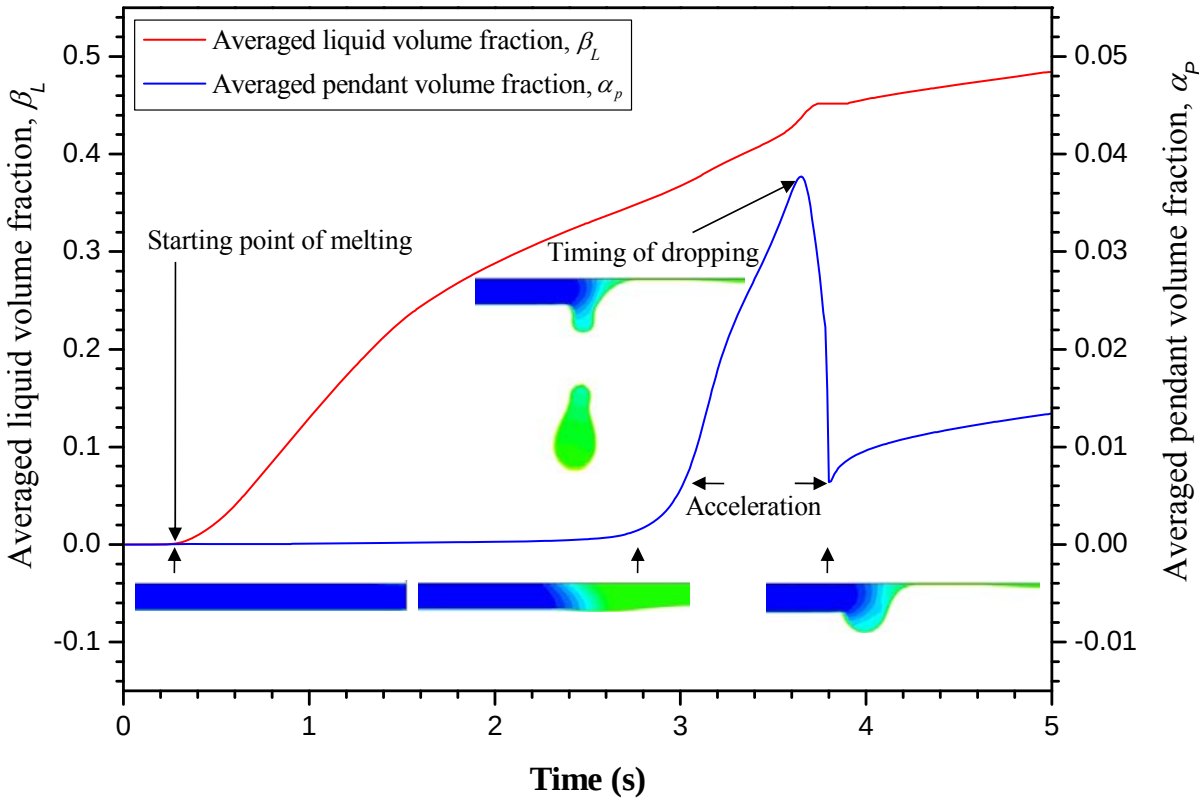

Fig. 5 Time-dependent averaged liquid volume fraction of PCM and averaged pendant volume fraction of PCM

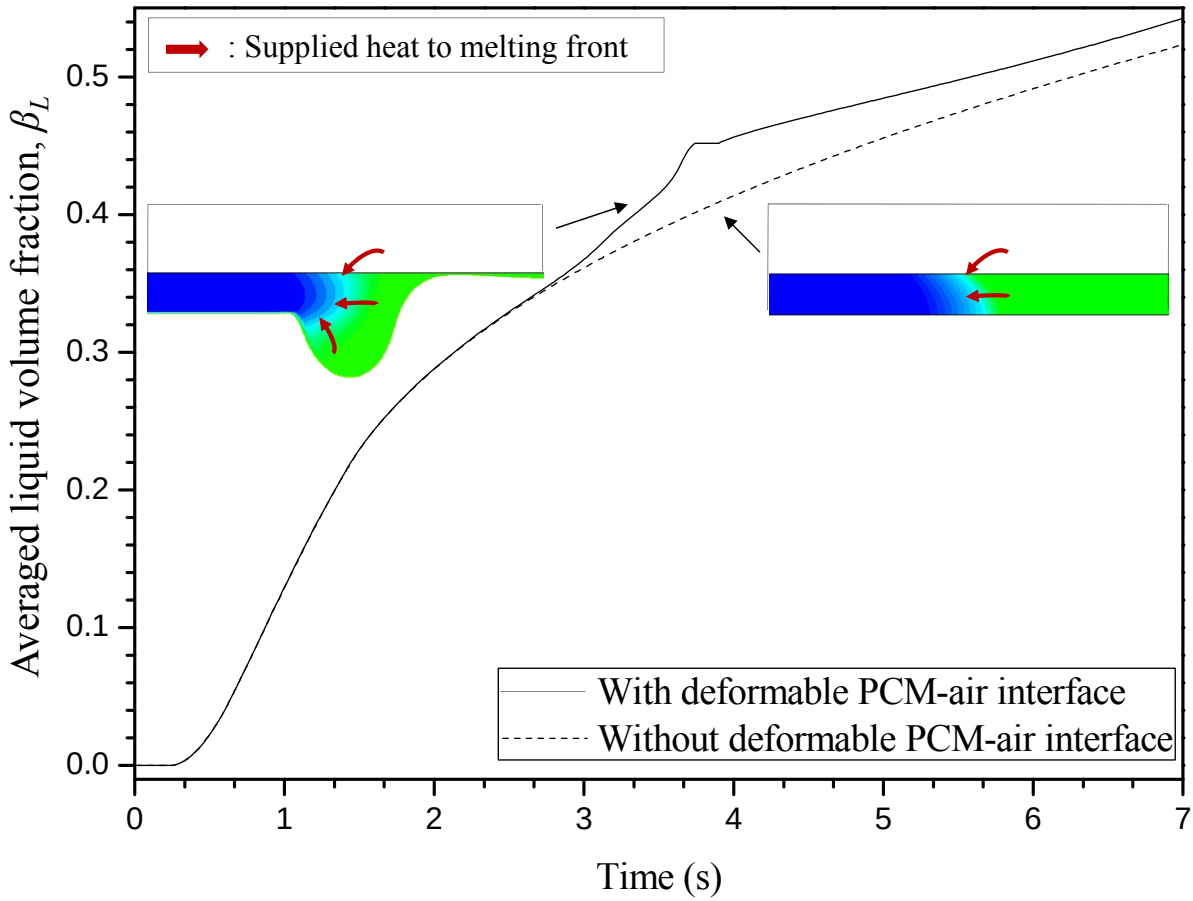

Fig. 6 Time-dependent averaged liquid volume fraction distribution with and without deformable PCM-air interface

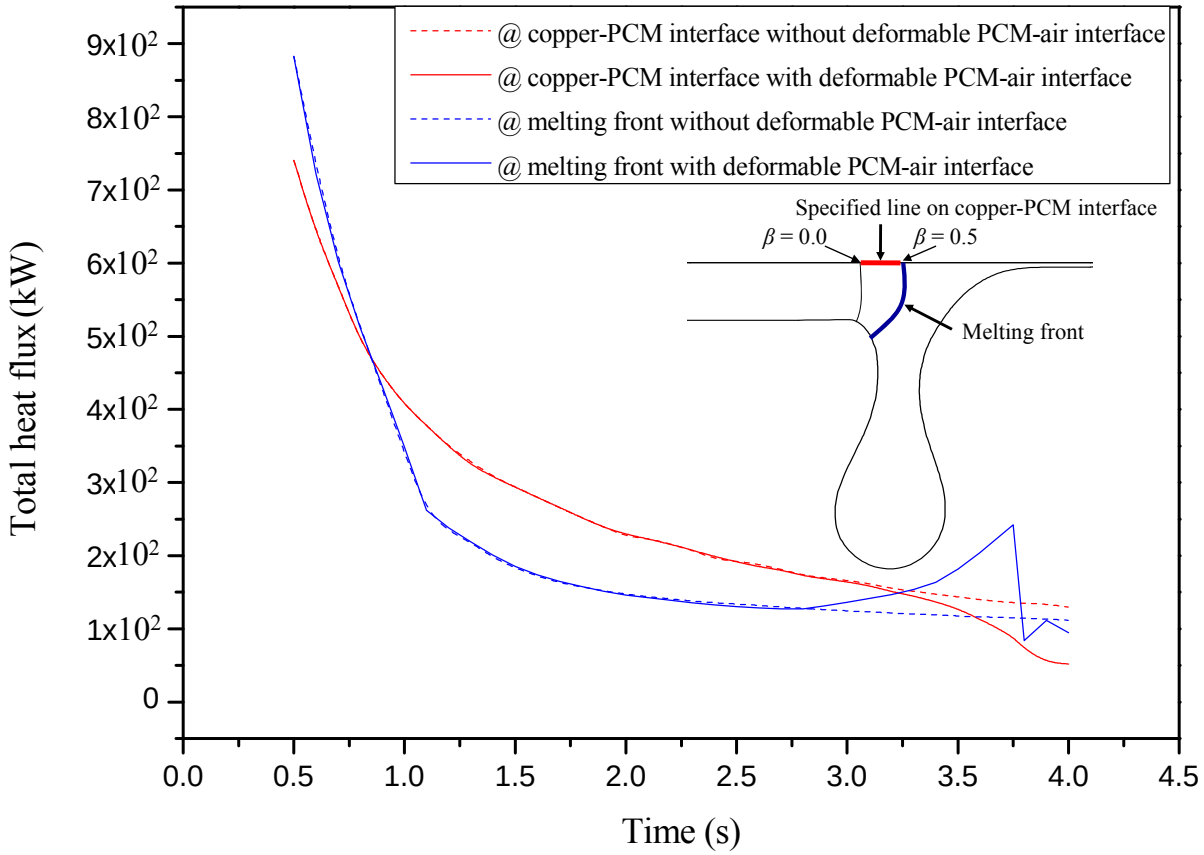

Fig. 7 Time-dependent heat flux at copper-PCM interface (black) and melting front (blue) with and without deformable PCM-air interface (For interpretation of the references to color in this figure legend, the reader is referred to the web version of this article)

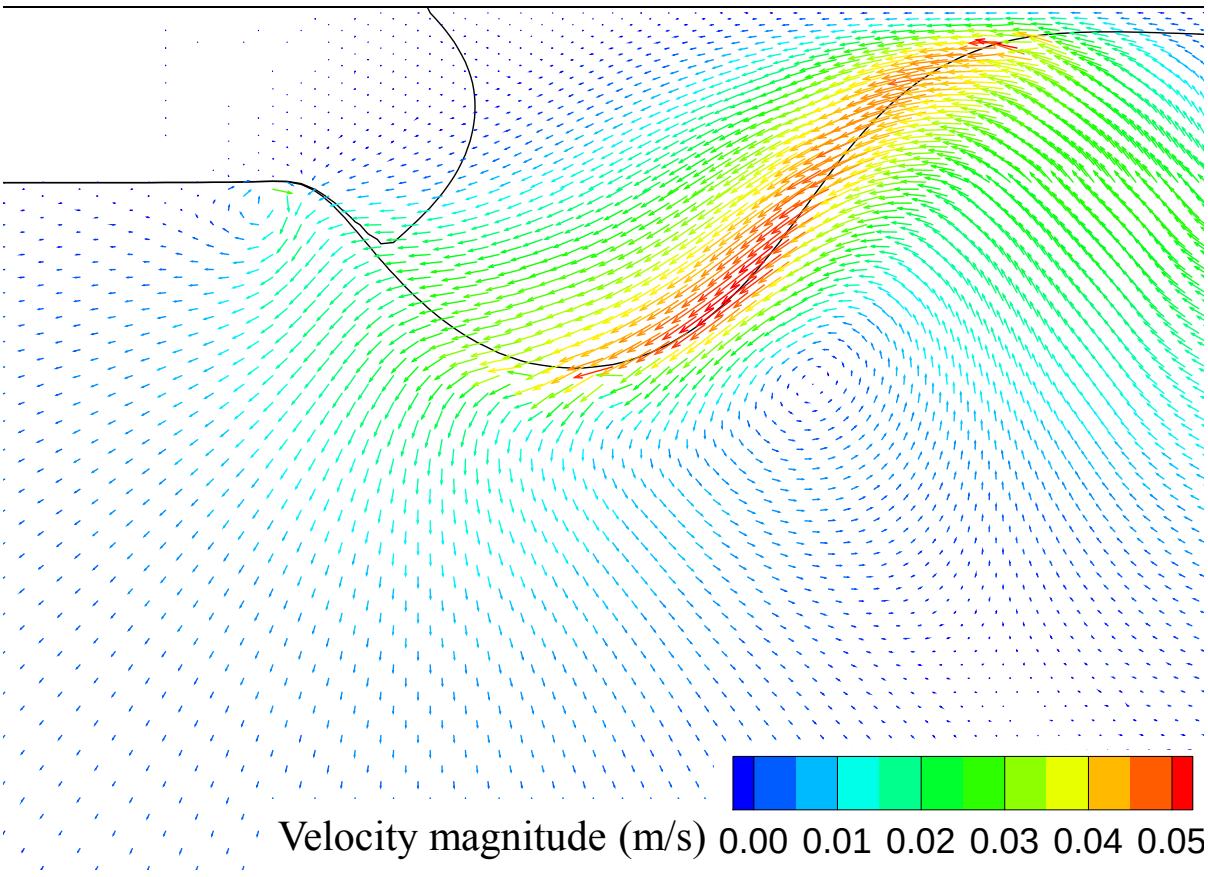

Fig. 8 Velocity distribution inside molten PCM at 3.3 s

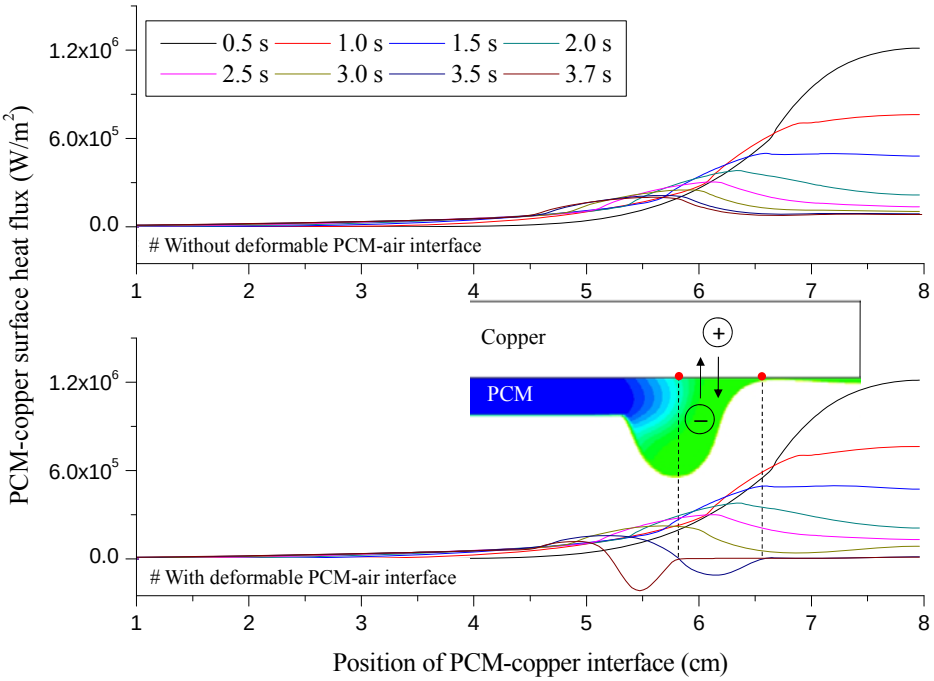

Fig. 9 Surface heat flux distribution along copper-PCM interface for cases (a) without and (b) with considering deformable PCM-air interface over time

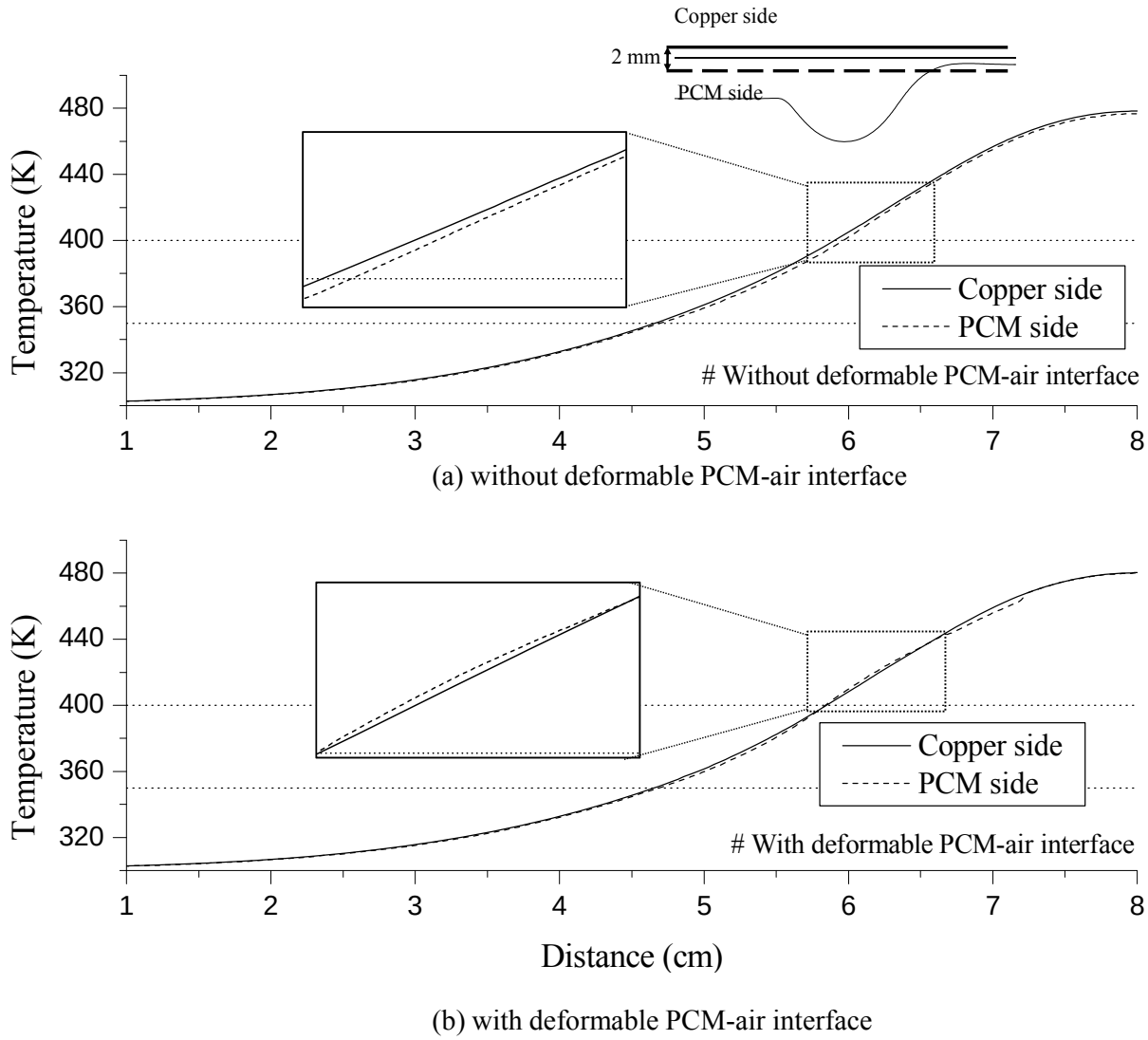

Fig. 10 Temperature at a point which is 1 mm away from copper-PCM interface toward copper side (solid line) and PCM side (dashed line) at 3.5 s

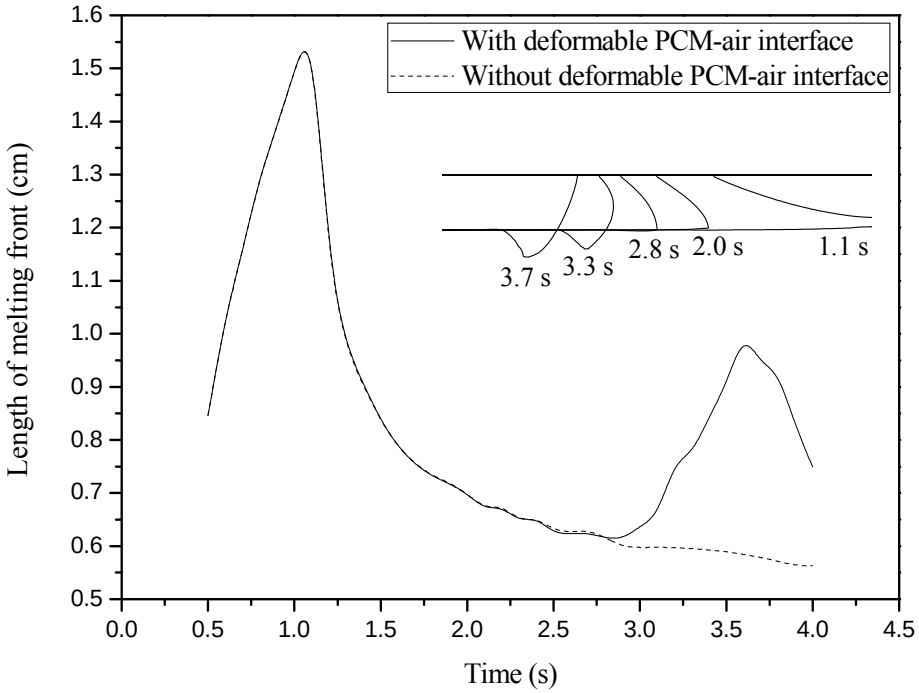

Fig. 11 Time-dependent distribution of the length of the melting front with and without a deformable PCM-air interface

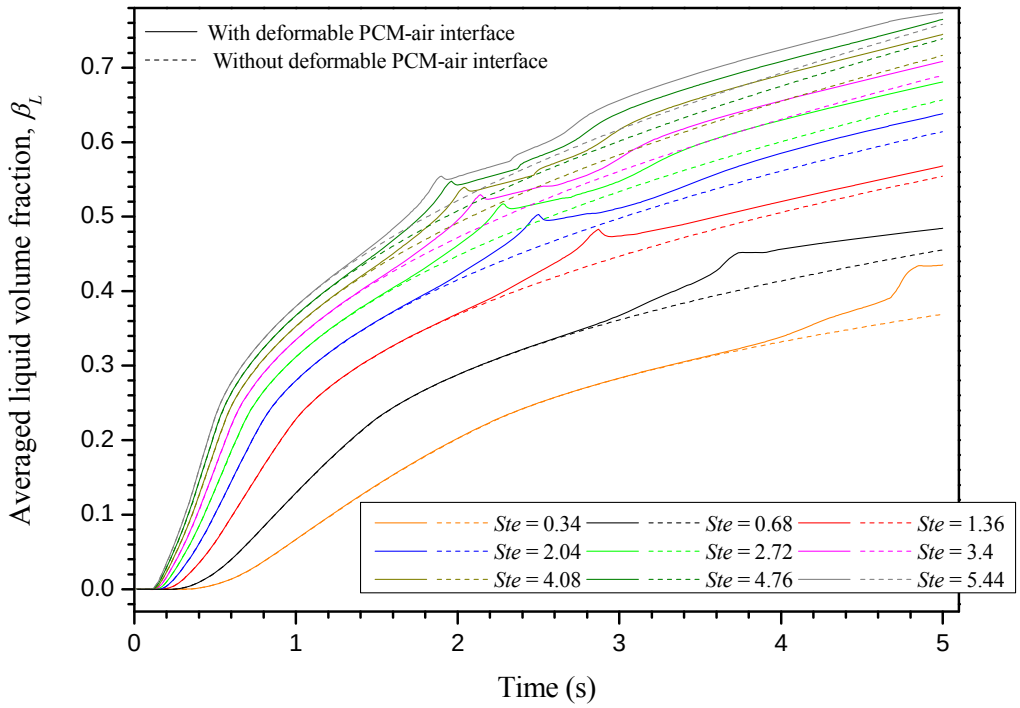

Fig. 12 Time-dependent liquid fraction distribution for various Stefan numbers at surface tension coefficient = 0.25

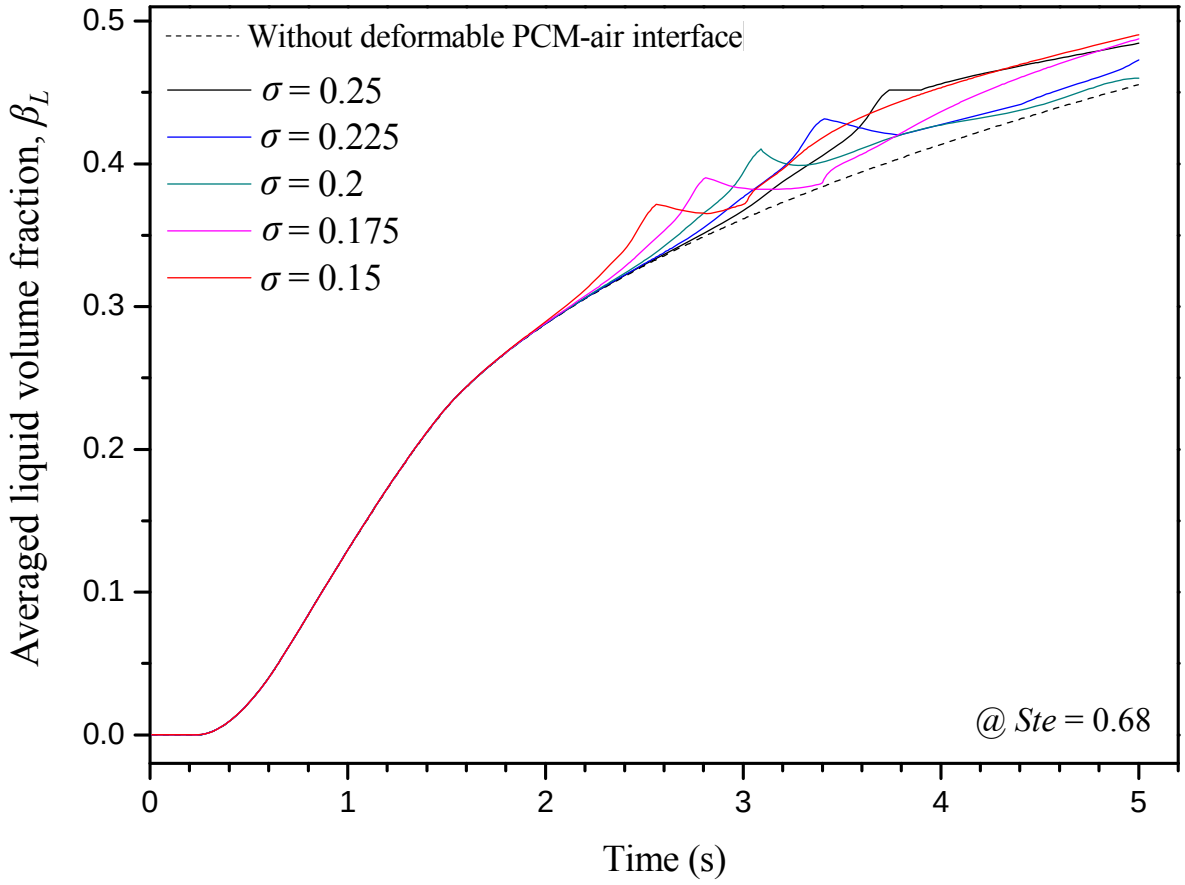

Fig. 13 Time-dependent liquid fraction distribution for various surface tension coefficient at Ste = 0.68

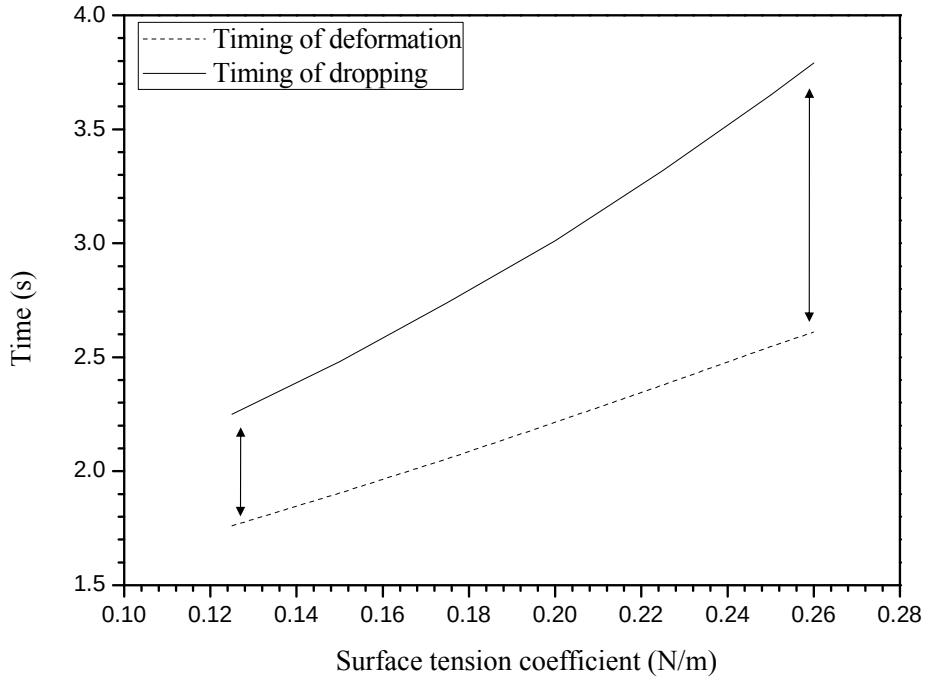

Fig. 14 Time for deformation and dropping according to surface tension coefficient at Ste = 0.68

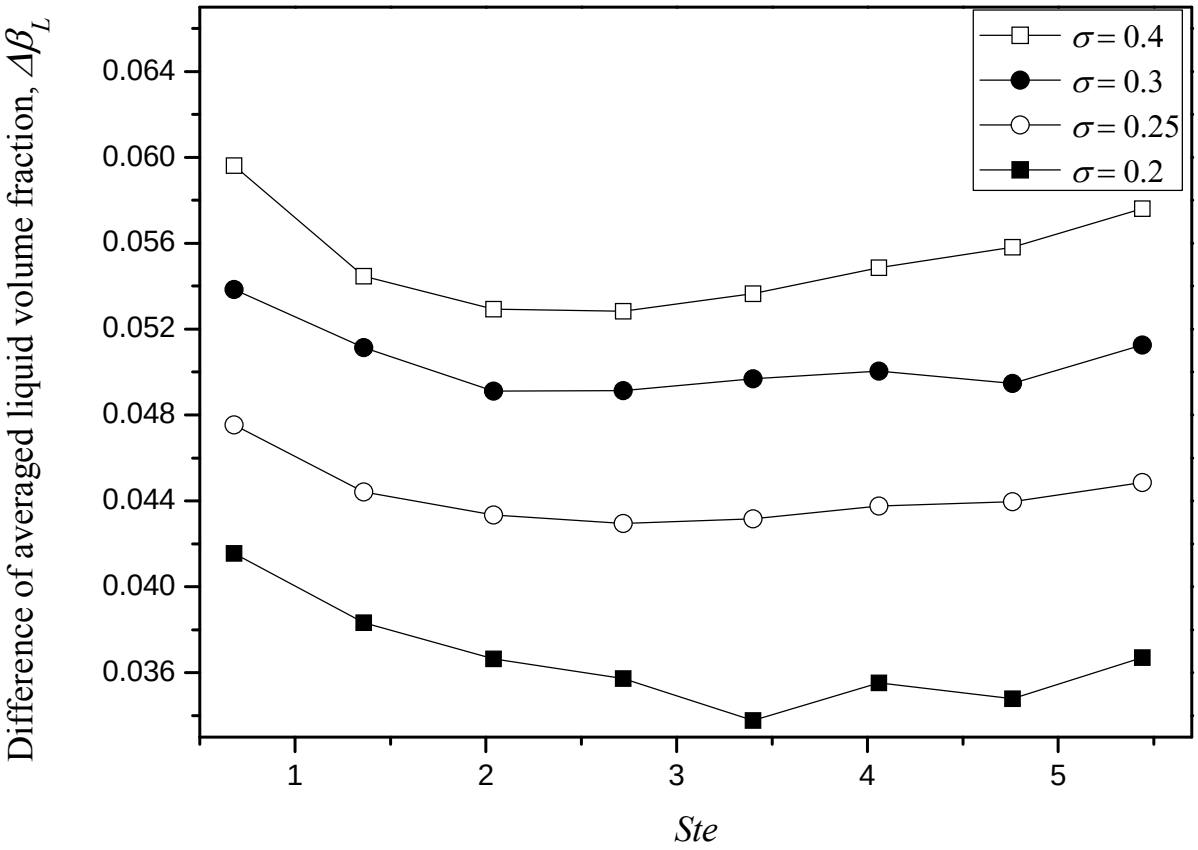

Fig. 15 Difference of averaged liquid volume fraction between cases of deformable and non-deformable PCM-air interface for various Stefan numbers and surface tension coefficients at the time of dropping

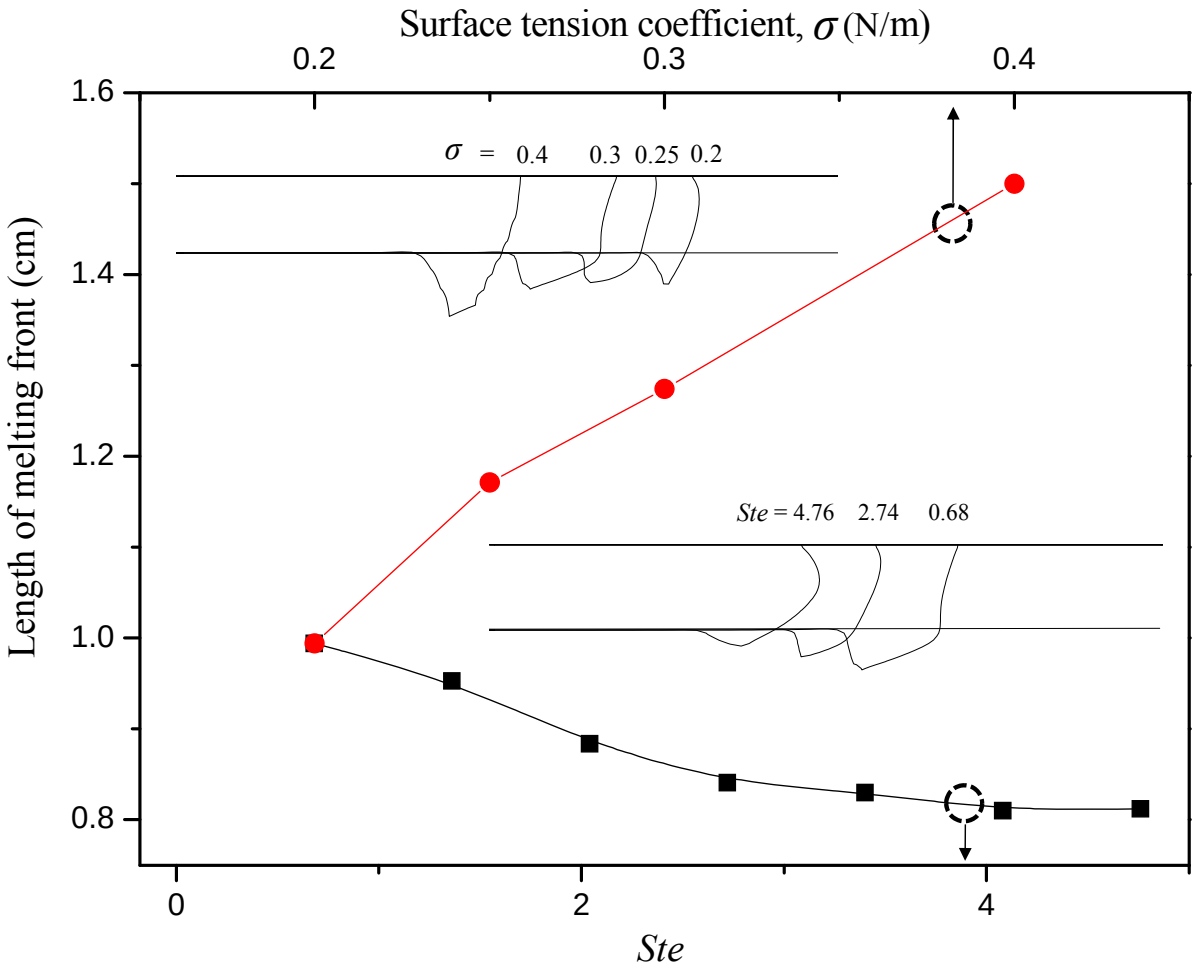

Fig. 16 Length of melting front according to surface tension coefficient and Stefan number at the time of dropping

Table 1 Physical properties used in the present calculation

Parameter	Symbol	Value	Units
Air (gas phase)			
Density	ρ_g	1.225	kg/m^3
Thermal conductivity	k_g	0.0242	W(m K)
Specific heat	$c_{p,g}$	1006.43	J/(kg K)
Viscosity	μ_g	1.789×10^{-5}	kg/(m s)
Copper (solid phase)			
Density	ρ_c	8978	kg/m^3

Thermal conductivity	k_c	387.6	W/(m K)
Specific heat	$c_{p,c}$	381	J/(kg K)
PCM (solid phase)			
Density	ρ_s	980	kg/m^3
Thermal conductivity	k_s	24	W/(m K)
Specific heat	$c_{p,s}$	1360	J/(kg K)
Latent heat of melting	L	1.8×10^5	J/kg
Melting temperature	T_m	400	K
PCM (liquid phase)			
Density	ρ_l	900	kg/m^3
Thermal conductivity	k_l	15	W/(m K)
Specific heat	$c_{p,l}$	680	J/(kg K)
Viscosity	μ_l	0.1	kg/(m s)
Solidification temperature	T_s	350	K